International Tables for Crystallography (2006). Vol. C, Figure 4.3.8.4, p. 422.

The axial three-beam fringes will coincide with the lattice planes, and show atom positions as dark if $\chi(u_{\mathbf{g}}) = (2n - 1/2)\pi$ and $\eta_0(t) - \eta_{\mathbf{g}}(t) = -\pi/2$. This total phase shift of $-\pi$ between Ψ_0 and the scattered beams is the desirable imaging condition for phase contrast, giving rise to dark atom positions on a bright background. This requires

$$C_s = (4n - 1)/(\lambda^3 u_{\mathbf{g}}^4) - 2\Delta f/(\lambda^2 u_{\mathbf{g}}^2)$$

as a condition for identical axial three-beam lattice images for $n = 0, 1, 2, \ldots$. This family of lines has been plotted in Fig. 4.3.8.3 for the (111) planes of silicon. Dashed lines denote the locus of 'white-atom' images (reversed contrast fringes), while the dotted lines indicate half-period images. In practice, the depth of field is limited by the finite illumination aperture θ_c, and few-beam lattice-image contrast will be a maximum at the stationary-phase focus setting, given by

$$\Delta f_0 = -C_s \lambda^2 u_{\mathbf{g}}^2. \qquad (4.3.8.11)$$

This choice of focus ensures $\nabla\chi(u) = 0$ for $u = u_{\mathbf{g}}$, and thus ensures the most favourable trade-off between increasing θ_c and loss of fringe contrast for lattice planes $\mathbf{g}$. Note that Δf_0 is not equal to the Scherzer focus Δf_s (see below). This focus setting is also indicated on Fig. 4.3.8.3, and indicates the instrumental conditions which produce the most intense (111) three- (or five-) beam axial fringes in silicon. For three-beam axial fringes of spacing d, it can be shown that the depth of field Δz is approximately

$$\Delta z = (\ln 2)^{1/2} d/\theta_c \pi. \qquad (4.3.8.12)$$

This depth of field, within which strong fringes will be seen, is indicated as a boundary on Fig. 4.3.8.3. Thus, the finer the image detail, the smaller is the focal range over which it may be observed, for a given illumination aperture θ_c.

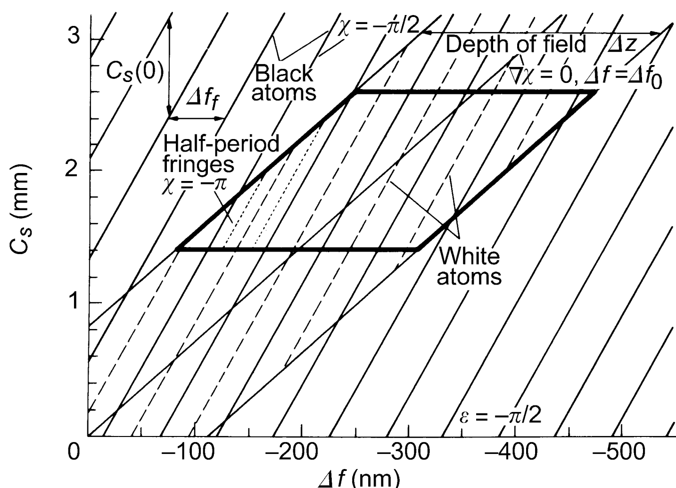

Fig. 4.3.8.3. A summary of three- (or five-) beam axial imaging conditions. Here, Δf_f is the Fourier image period, Δf_0 the stationary-phase focus, $C_s(0)$ the image period in C_s, and a scattering phase of $-\pi/2$ is assumed. The lines are drawn for the (111) planes of silicon at 100 kV with $\theta_c = 1.4$ mrad.

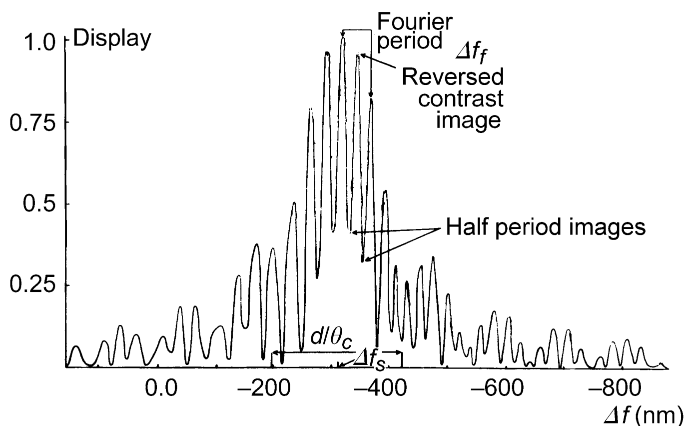

Fig. 4.3.8.4. The contrast of few-beam lattice images as a function of focus in the neighbourhood of the stationary-phase focus [see Olsen & Spence (1981)].

Fig. 4.3.8.4 shows an exact dynamical calculation for the contrast of three-beam axial fringes as a function of Δf in the neighbourhood of Δf_0. Both reversed contrast and half-period fringes are noted. The effects of electronic instabilities on lattice images are discussed in Subsection 4.3.8.3. It is assumed above that θ_c is sufficiently small to allow the neglect of any changes in diffraction conditions (Ewald-sphere orientation) within Θ_c. Under a similar approximation but without the approximations of transfer theory, Desseaux, Renault & Bourret (1977) have analysed the effect of beam divergence on two-dimensional five-beam axial lattice fringes.

When two-dimensional patterns of fringes are considered, the Fourier imaging conditions become more complex (see Subsection 4.3.8.3), but half-period fringe systems and reversed-contrast images are still seen. For example, in a cubic projection, a focus change of $\Delta f_f/2$ results in an image shifted by half a unit cell along the cell diagonal. It is readily shown that

$$\exp[i\chi(\Delta f)] = \exp[i\chi(\Delta f + \Delta f_f)]$$

if $\Delta f_f = 2na^2/\lambda + 2mb^2/\lambda$ when n, m are integers and a and b are the two dimensions of any orthogonal unit cell that can be chosen for $\Psi_p(x, y)$. Thus, changes in focus by $\Delta f_f(n, m)$ produce identical images in crystals for which such a cell can be chosen, regardless of the number of beams contributing (Cowley & Moodie, 1960).

For closed-form expressions for the few-beam (up to 10 beams) two-dimensional dynamical Bragg-beam amplitudes $\Psi_{\mathbf{g}}$ in orientations of high symmetry, the reader is referred to the work of Fukuhara (1966).

4.3.8.3. *Crystal structure images*

We define a crystal structure image as a high-resolution electron micrograph that faithfully represents a projection of a crystal structure to some limited resolution, and which was obtained using instrumental conditions that are independent of the structure, and so require no *a priori* knowledge of the structure. The resolution of these images is discussed in Subsection 4.3.8.6, and their variation with instrumental parameters in Subsection 4.3.8.4.

Equation (4.3.8.2) must now be modified to take account of the finite electron source size used and of the effects of the range of energies present in the electron beam. For a perfect crystal we may write, as in equation (2.5.1.36) in *IT* B (1992),

$$I_T(\mathbf{r}) = \textstyle\iint |\psi(\mathbf{u}', \Delta f, \mathbf{r})|^2 \, G(\mathbf{u}') B(\Delta f, \mathbf{u}') \, \mathrm{d}\mathbf{u}' \, \mathrm{d}\Delta f \qquad (4.3.8.13a)$$

for the total image intensity due to an electron source whose normalized distribution of wavevectors is $G(\mathbf{u}')$, where $\mathbf{u}'$ has components u_1, v_1, and which extends over a range of energies corresponding to the distribution of focus $B(\Delta f, \mathbf{u})$. If χ is also assumed to vary linearly across θ_c and changes in the diffraction conditions over this range are assumed to make only negligible changes in the diffracted-beam amplitude $\Psi_{\mathbf{g}}$, the expression for a Fourier coefficient of the total image intensity $I_T(\mathbf{r})$ becomes

Copyright © 2006 International Union of Crystallography

references